Generation and manipulation of Schrödinger cat states in Rydberg atom arrays

A. Omran,[1,*] H. Levine,[1,*] A. Keesling,[1] G. Semeghini,[1] T. T. Wang,[1,2] S. Ebadi,[1] H. Bernien,[3] A. S. Zibrov,[1] H. Pichler,[1,4] S. Choi,[5] J. Cui,[6] M. Rossignolo,[7] P. Rembold,[6] S. Montangero,[8] T. Calarco,[6,9] M. Endres,[10] M. Greiner,[1] V. Vuletić,[11] and M. D. Lukin[1,†]

[1]*Department of Physics, Harvard University, Cambridge, MA 02138, USA*
[2]*Department of Physics, Gordon College, Wenham, MA 01984, USA*
[3]*Institute for Molecular Engineering, University of Chicago, Chicago, IL 60637, USA*
[4]*ITAMP, Harvard-Smithsonian Center for Astrophysics, Cambridge, MA 02138, USA*
[5]*Department of Physics, University of California Berkeley, Berkeley, CA 94720, USA*
[6]*Forschungszentrum Jülich, Institute of Quantum Control (PGI-8), D-52425 Jülich, Germany*
[7]*Institute for Quantum Optics and IQST Center, Universität Ulm, D-89081 Ulm, Germany*
[8]*Dipartimento di Fisica e Astronomia "G. Galilei", Università degli Studi di Padova & INFN, I-35131 Italy*
[9]*Institute for Theoretical Physics, University of Cologne, D-50937 Cologne, Germany*
[10]*Division of Physics, Mathematics and Astronomy, California Institute of Technology, Pasadena, CA 91125, USA*
[11]*Department of Physics and Research Laboratory of Electronics, Massachusetts Institute of Technology, Cambridge, MA 02139, USA*

Quantum entanglement involving coherent superpositions of macroscopically distinct states is among the most striking features of quantum theory, but its realization is challenging because such states are extremely fragile. Using a programmable quantum simulator based on neutral atom arrays with interactions mediated by Rydberg states, we demonstrate the creation of "Schrödinger cat" states of the Greenberger-Horne-Zeilinger (GHZ) type with up to 20 qubits. Our approach is based on engineering the energy spectrum and using optimal control of the many-body system. We further demonstrate entanglement manipulation by using GHZ states to distribute entanglement to distant sites in the array, establishing important ingredients for quantum information processing and quantum metrology.

Greenberger-Horne-Zeilinger (GHZ) states constitute an important class of entangled many-body states [1]. Such states provide an important resource for applications ranging from quantum metrology [2] to quantum error correction [3]. However, these are among the most fragile many-body states because a single error on any one of the N qubits collapses the superposition, resulting in a statistical mixture. Remarkably, despite their highly entangled nature, GHZ states can be characterized by just two diagonal and two off-diagonal terms in the N-particle density matrix. In contrast to quantifying the degree of entanglement in general many-body states, which is extremely challenging [4–6], the GHZ state fidelity ($\mathcal{F} > 0.5$) constitutes an accessible witness for N-partite entanglement [7]. For these reasons, GHZ state creation can serve as an important benchmark for characterizing the quality of any given quantum hardware. Such states have been previously generated and characterized by using systems of nuclear spins [8, 9], individually controlled optical photons [10–12], trapped ions [7, 13–15], and superconducting quantum circuits [16, 17]. Large-scale superposition states have also been generated in systems of microwave photons [18] and atomic ensembles without individual particle addressing [2].

Here, we demonstrate the preparation of N-particle GHZ states

$$|\mathrm{GHZ}_N\rangle = \frac{1}{\sqrt{2}}\left(|0101\cdots\rangle + |1010\cdots\rangle\right) \qquad (1)$$

in a one dimensional array of individually trapped neutral ^{87}Rb atoms, in which the qubits are encoded in an atomic ground state $|0\rangle$ and a Rydberg state $|1\rangle$ (phase convention is provided in [27]). Our entangling operation relies on the strong van-der-Waals interaction between atoms in states $|1\rangle$ and on engineering the energy spectrum of the quantum many-body system to allow for a robust quantum evolution from an initial product state to a GHZ state. For both generating and characterizing GHZ states (Fig. 1), all the atoms were homogeneously coupled to the Rydberg state $|1\rangle$ by means of a two-photon transition with an effective coupling strength $\Omega(t)$ and detuning $\Delta(t)$ [19, 20]. In addition, we used addressing beams to introduce local energy shifts δ_i on specific sites i along the array (Fig. 1A). The resulting many-body Hamiltonian is

$$\frac{H}{\hbar} = \frac{\Omega(t)}{2}\sum_{i=1}^{N}\sigma_x^{(i)} - \sum_{i=1}^{N}\Delta_i(t)n_i + \sum_{i<j}\frac{V}{|i-j|^6}n_i n_j \qquad (2)$$

where $\sigma_x^{(i)} = |0\rangle\langle 1|_i + |1\rangle\langle 0|_i$ is the qubit flip operator, $\Delta_i(t) = \Delta(t) + \delta_i$ is the local effective detuning set by the Rydberg laser and the local light shift, $n_i = |1\rangle\langle 1|_i$ is the number of Rydberg excitations on site i, and V is the interaction strength of two Rydberg atoms on neighboring sites. The separation between adjacent sites was chosen so that the nearest-neighbor interaction $V = 2\pi \cdot 24\,\mathrm{MHz} \gg \Omega$ results in the Rydberg blockade [21–23], forbidding the simultaneous excitation of adjacent atoms into the state $|1\rangle$.

To prepare GHZ states, we uesd arrays with an even

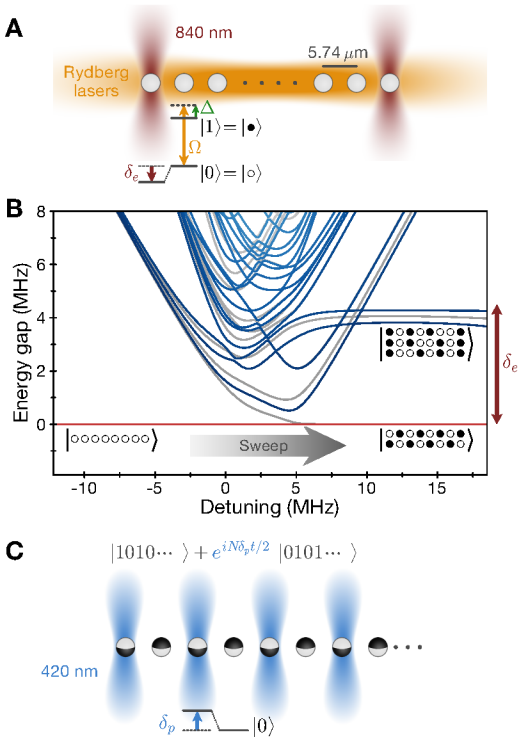

FIG. 1. Experimental scheme and entanglement procedure. **A,** ^{87}Rb atoms initially in a ground state $|0\rangle = |5S_{1/2}, F = 2, m_F = -2\rangle$ are coupled to a Rydberg state $|1\rangle = |70S_{1/2}, m_J = -1/2\rangle$ by a light field with a coupling strength $\Omega/(2\pi) \leq 5$ MHz and a variable detuning Δ. Local addressing beams at 840 nm target the edge atoms, reducing the energy of $|0\rangle$ at those sites by a light shift δ_e. **B,** Many-body energy gap spectrum of $N = 8$ atoms, including energy shifts on the edge atoms. For positive detuning, the states with one ground state atom on the edges are favored over states with a Rydberg atom on both edges. An adiabatic pathway connects the state $|G_N\rangle = |000\cdots\rangle$ with the two GHZ components. Gray lines in the spectrum are energies associated with antisymmetric states, which are not coupled to the initial state by Hamiltonian (2). **C,** Method to control the phase ϕ of GHZ states. Every other site of the array is illuminated with a local addressing beam at 420 nm, which imposes a negative differential light shift δ_p on the $|0\rangle$-to-$|1\rangle$ transition. The offset in state $|0101\cdots\rangle$ relative to $|1010\cdots\rangle$ leads to an evolving dynamical phase.

number N of atoms. For large negative detuning Δ of the Rydberg laser, the many-body ground state of the Hamiltonian (2) is $|G_N\rangle = |0000\cdots\rangle$. For large uniform positive detuning $\Delta_i = \Delta$, the ground-state manifold consists of $N/2 + 1$ nearly degenerate classical configurations with $N/2$ Rydberg excitations. These include in particular the two target antiferromagnetic configurations $|A_N\rangle = |0101\cdots01\rangle$ and $|\overline{A}_N\rangle = |1010\cdots10\rangle$ [24], as well as other states with nearly identical energy (up to a weak second-nearest neighbor interaction), with both edges excited, such as $|10010\cdots01\rangle$. To isolate a coherent superposition of states $|A_N\rangle$ and $|\overline{A}_N\rangle$, we introduced local light shifts δ_e using off-resonant laser beams at 840 nm, generated with an acousto-optic deflector (AOD), which energetically penalize the excitation of edge atoms (Fig. 1A), and effectively eliminate the contribution of undesired components. In this case, the ground state for positive detuning is given by the GHZ state (1) and there exists in principle an adiabatic pathway that transforms the state $|G_N\rangle$ into $|\mathrm{GHZ}_N\rangle$ by adiabatically increasing $\Delta(t)$ from negative to positive values (Fig. 1B).

In practice, the time necessary to adiabatically prepare such a GHZ state grows with system size and becomes prohibitively long for large N, owing to small energy gaps in the many-body spectrum. To address this limitation, we used optimal control methods to find laser pulses that maximize the GHZ state preparation fidelity while minimizing the amount of time necessary. Our specific implementation, the remote dressed chopped-random basis algorithm (RedCRAB) [25, 26], yields optimal shapes of the laser intensity and detuning for the given experimental conditions [27]. For $N \leq 8$ atoms, we performed this optimization using $\delta_e/(2\pi) \approx -4.5$ MHz light shifts on the edge atoms. For larger systems of $N > 8$, the preparation was found to be more robust by increasing the edge light shifts to $\delta_e/(2\pi) \approx -6$ MHz and adding $\delta_{4,N-3}/(2\pi) \approx -1.5$ MHz light shifts on the third site from both edges.

Our experiments are based on the optical tweezer platform and experimental procedure described previously [20]. After the initialization of a defect-free N-atom array, the traps were switched off while the atoms were illuminated with the Rydberg and local light shift beams. The internal state of the atoms is subsequently measured by imaging state $|0\rangle$ atoms recaptured in the traps, while Rydberg atoms are repelled by the trapping light [28]. The results of such experiments for a 20-atom array are demonstrated in Fig. 2. After applying the optimized pulse shown in Fig. 2B, we measured the probability of observing different patterns $p_n = \langle n|\,\rho\,|n\rangle$ in the computational basis, where ρ is the density operator of the prepared state. The measured probability to observe each one of the 2^{20} possible patterns in a 20-atom array is shown in Fig. 2A. The states $|A_{20}\rangle$ and $|\overline{A}_{20}\rangle$ clearly stand out (Fig. 2A, blue bars) with a combined probability of 0.585(14) and almost equal probability of observing each one.

To characterize the experimentally prepared state ρ, we evaluated the GHZ state fidelity

$$\mathcal{F} = \langle \mathrm{GHZ}_N|\,\rho\,|\mathrm{GHZ}_N\rangle = \frac{1}{2}\left(p_{A_N} + p_{\overline{A}_N} + c_N + c_N^*\right) \tag{3}$$

where p_{A_N} and $p_{\overline{A}_N}$ are the populations in the target components and $c_N = \langle \overline{A}_N|\,\rho\,|A_N\rangle$ is the off-diagonal

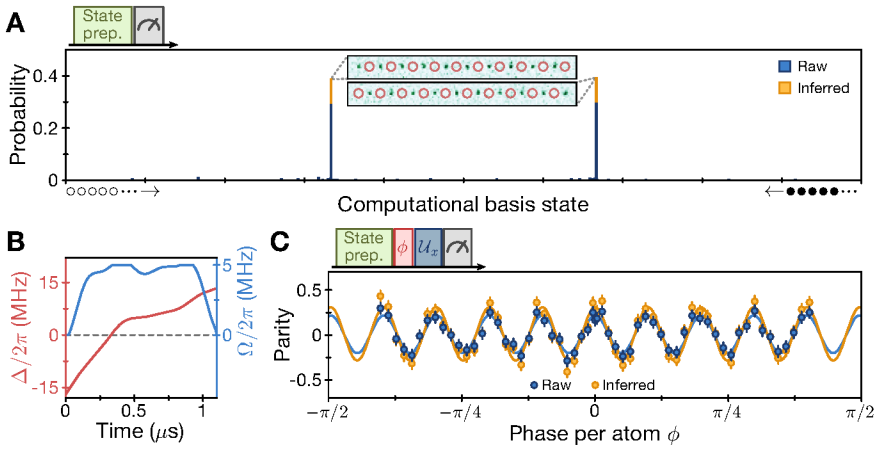

FIG. 2. Characterization of a 20-atom GHZ state. **A,** Probability of observing different patterns, showing a large population of the two target patterns out of $2^{20} = 1,048,576$ possible states. Shown here are the raw measured values (blue bars) and the populations inferred by using maximum likelihood estimation (orange bars) for the two target states. (Insets) fluorescence images of the two target patterns, where red circles mark empty sites corresponding to atoms in state $|1\rangle$. **B,** Optimal control pulse used for state preparation. **C,** Parity oscillations produced by acquiring a relative phase between the GHZ components. We apply a staggered field with a shift of $\delta_p/(2\pi) = \pm 3.8\,\mathrm{MHz}$ on all sites, followed by an operation $\mathcal{U}_x$ so that subsequent parity measurements are sensitive to ϕ [27]. From the population measurement and the oscillation amplitude, we infer a lower bound on the 20-atom GHZ fidelity of $\mathcal{F} \geq 0.542(18)$. Error bars denote 68% confidence intervals.

matrix element, which can be measured by using the maximal sensitivity of the GHZ state to a staggered magnetic field. Specifically, evolving the system with the Hamiltonian $H_p = \hbar\delta_p/2 \sum_{i=1}^{N} (-1)^i \sigma_z^{(i)}$, the amplitude c_N acquires a phase ϕ at a rate of $\dot{\phi} = N\delta_p$. Measuring an observable that oscillates at this frequency provides a lower bound on the coherence $|c_N|$ through the oscillation contrast [27, 29]. In our experiments, the staggered field was implemented by applying off-resonant focused beams of equal intensity at 420 nm, generated by another AOD, to every other site of the array (Fig. 1C), resulting in a local energy shift δ_p [27]. Subsequently, we drove the atoms resonantly, applying a unitary operation $\mathcal{U}_x$ in order to change the measurement basis [27], so that a measurement of the parity $\mathcal{P} = \prod_i \sigma_z^{(i)}$ becomes sensitive to the phase of c_N. The measured parity is shown in Fig. 2C as a function of the phase accumulated on each atom, demonstrating the coherence of the created state.

To extract the entanglement fidelity for large atomic states, we carefully characterized our detection process used to identify atoms in $|0\rangle$ and $|1\rangle$ because it has a small but finite error. We have independently determined the probability to misidentify the state of a particle to be $p(1|0) = 0.0063(1)$, and $p(0|1) = 0.0227(42)$ [27]. Subsequently, we use a maximum-likelihood estimation procedure to infer the properties of created states on the basis of the raw measurement results. Using this procedure, we infer a probability of preparing states $|A_{20}\rangle$ and $|\overline{A}_{20}\rangle$ to be 0.782(32) (Fig. 2A, orange bars) and an amplitude of oscillation of 0.301(18) (Fig. 2C, orange points). From these measurements, we extracted a lower bound for the 20-atom GHZ state fidelity of $\mathcal{F} \geq 0.542(18)$.

This protocol was applied for multiple system sizes of $4 \leq N \leq 20$, using 1.1 μs control pulses optimized for each N individually. Consistent with expected GHZ dynamics (Fig. 1C) [13], the frequency of the measured parity oscillations grows linearly with N (Fig. 3A). Extracting the GHZ fidelity from these measurements shows that we surpass the threshold of $\mathcal{F} = 0.5$ for all system sizes studied (Fig. 3B and table S1). We further characterized the lifetime of the created GHZ state by measuring the parity signal after a variable delay (Fig. 3C). These observations are most consistent with Gaussian decay, while characteristic lifetimes are reduced relatively slowly for increasing system sizes, indicating the presence of a non-Markovian environment [3, 14].

As an application of our entanglement manipulation technique, we demonstrate its use for entanglement distribution between distant atoms. Specifically, we consider the preparation of Bell states between atoms at the two opposite edges of the array. Our approach was based on first creating the GHZ state by using the above procedure, followed by an operation that disentangles all but two target atoms. The latter is realized by shifting the transition frequencies of the two target edge atoms by using two strong, blue-detuned addressing beams at 420 nm. Subsequently, we performed a reverse detuning sweep of the Rydberg laser that effectively disentangles all atoms except those at the edges. The resulting state corresponds to a coherent superposition of two pinned excitations that can be converted into a Bell state

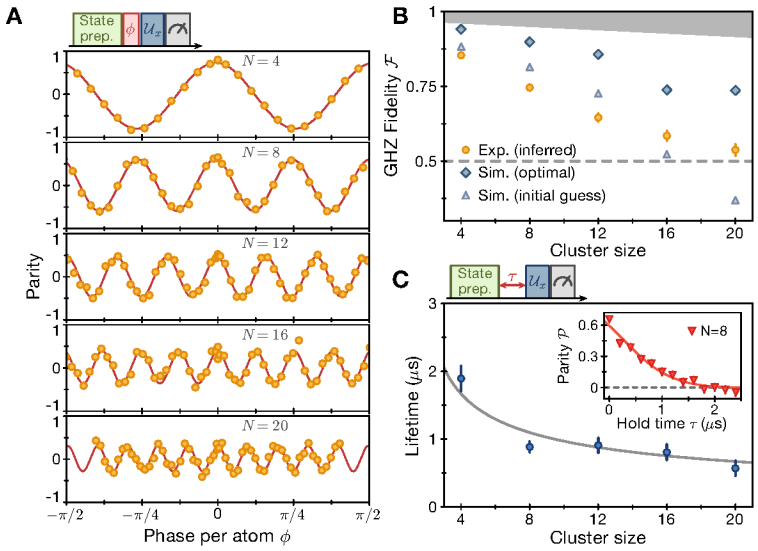

FIG. 3. Quantifying entanglement for different system sizes. **A,** Parity oscillations measured on different system sizes. We apply a staggered field with a shift of $\delta_p/(2\pi) = \pm 3.8$ MHz on all sites and observe a scaling of the phase accumulation rate proportional to the system size N. **B**, Inferred GHZ fidelity for different system sizes (orange circles) [27]. Blue diamonds show the result of simulations that account for dephasing during state preparation, decay from off-resonant photon scattering, and imperfect detection of coherence through parity oscillations [27]. Pale blue triangles show identical simulations for the initial guess pulses for the RedCRAB optimization, consisting of a $T = 1.1\,\mu$s linear detuning sweep and $\Omega(t) = \Omega_{\max}[1-\cos^{12}(\pi t/T)]$. The gray shaded area marks a region not measurable with our parity observable [27]. **C**, Lifetime of the GHZ state coherence. For all system sizes N, we measure the state parity after a variable delay following the GHZ state preparation, which (inset) decays to zero. We fit the individual parity data to the tail of a Gaussian decay curve because we assume that the dephasing started during state preparation - before $\tau = 0$. The gray line shows a theoretical prediction with no free parameters, accounting for known dephasing mechanisms in our system.

$|\Phi^+\rangle = (|00\rangle + |11\rangle)/\sqrt{2}$ by applying a resonant $\pi/2$ pulse on the edge atoms (Fig. 4A).

To demonstrate this protocol experimentally, we prepare a GHZ-state of 8 atoms, and turn on the detuned 420 nm addressing beams on the edge atoms, resulting in a shift of $\delta_{1,8}/(2\pi) = 6$ MHz. We then used an optimized Rydberg laser pulse to distribute the entanglement and observed the patterns $|00000000\rangle$ and $|10000001\rangle$ with a total probability of 0.729(9) after accounting for detection errors (Fig. 4B). We verified the coherence of the remote Bell pair by applying an additional $\pi/2$ pulse with a variable laser phase, and observed parity oscillations with an amplitude of 0.481(24) (Fig. 4C). Combining these results, we obtained the edge atom Bell state fidelity of 0.605(13).

Regarding our experimental observations, the optimal control provides a substantial improvement over naïve analytic pulses (Fig. 3B), while bringing our protocol close to the speed set by a more conventional protocol of building up entanglement through a series of two-qubit operations [27]. By contrast, a simple linear detuning sweep only allows for the creation of GHZ states for $N \leq 16$ within a fixed 1.1 μs window (Fig. 3B), even under ideal conditions. Our analysis reveals that the reason for this improvement stems from diabatic excitations and de-excitations in the many-body spectrum, related to the recently proposed mechanisms for quantum optimization speedup [27, 30, 31].

The measured entanglement fidelity is partially limited by imperfect qubit rotations used for parity measurements. Specifically, the qubit rotation operation $\mathcal{U}_x$ in our experiment is induced by an interacting Hamiltonian, which complicates this step [27]. The resulting evolution can be understood in terms of quantum many-body scars [20, 32], which gives rise to coherent qubit rotations, even in the presence of strong interactions. The deviations from an ideal parity measurement arise from the Rydberg blockade constraint and long-range interactions [27]. These grow with the system size, resulting in finite fidelities even for a perfect initial GHZ state (Fig. 3B, gray shaded area). Our quoted fidelity values do not include the correction for this imperfection and represent the lower bound on the actual GHZ state fidelities.

Entanglement generation, manipulation and lifetime are further limited by several sources of decoherence. The finite temperature of the atoms leads to random Doppler shifts on every site as well as position fluctuations that influence interaction energies. These thermal dephasing mechanisms lead to a Gaussian decay of the GHZ state

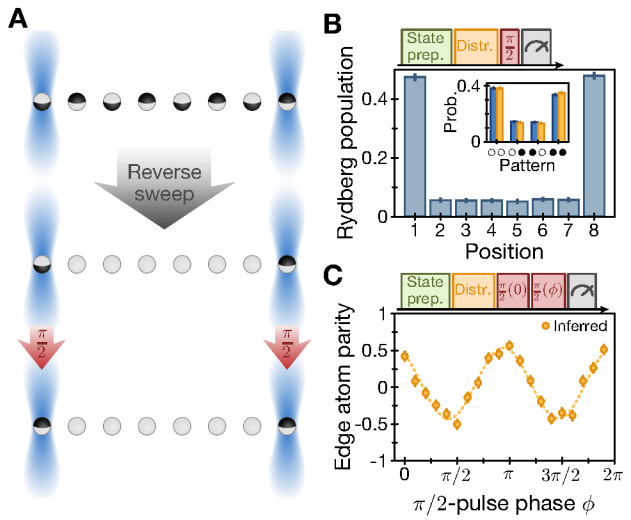

FIG. 4. Demonstration of entanglement distribution. **A,** Experimental protocol for $N = 8$. Edge atoms are addressed by light shift beams, and a reverse sweep of the Rydberg laser detuning is performed to disentangle the bulk of the array, leaving a Bell state $|\Psi^+\rangle \propto |1\cdots0\rangle + |0\cdots1\rangle$ on the edge. A $\pi/2$ pulse resonant only with the edge atoms is applied to convert the state $|\Psi^+\rangle$ to $|\Phi^+\rangle \propto |0\cdots0\rangle + |1\cdots1\rangle$. **B,** Measured Rydberg populations on each site after entanglement distribution. (Inset) Probabilities for different patterns on the edge atoms, which are consistent with the Bell state $|\Phi^+\rangle$. Blue bars show the raw data, while orange bars are the statistically inferred probabilities given our detection errors. **C,** Measurement of the Bell state coherence. GHZ entanglement is distributed to the edges, and a $\pi/2$ pulse is applied at laser phase $\phi = 0$, followed by a second $\pi/2$ pulse at varying phase ϕ. The amplitude of the parity oscillation provides a lower bound on the coherence of the Bell state, yielding a fidelity of $\mathcal{F} \geq 0.605(13)$.

coherence, whose time scale decreases with the system size as $1/\sqrt{N}$, which is in good agreement with our observations (Fig. 3C). Additionally, off-resonant laser scattering introduces a small rate of decoherence on each site in the array. We find that numerical simulations of the state preparation accounting for these imperfections predict higher GHZ fidelities than those obtained experimentally (Fig. 3B) [27]. We can attribute this discrepancy to several additional sources of errors. Laser phase noise likely contributes to the finite fidelity of the state preparation. Drifts in the beam positions of the Rydberg lasers can lead to changing light shifts, giving rise to uncontrolled detunings, and drifts in the addressing beam positions can lead to an imbalance in the local energy shifts and thereby in the populations of the two GHZ components, limiting the maximum possible coherence. This analysis highlights the utility of GHZ states for uncovering sources of errors. We emphasize that all of these known error sources can be mitigated through technical improvements [27].

Our experiments demonstrate a new promising approach for the deterministic creation and manipulation of large-scale entangled states, enabling the realization of GHZ-type entanglement in system sizes of up to $N = 20$ atoms. These results show the utility of this approach for benchmarking quantum hardware, demonstrating that Rydberg atom arrays constitute a competitive platform for quantum information science and engineering. Specifically, the entanglement generation and distribution could potentially be used for applications that range from quantum metrology and quantum networking to quantum error correction and quantum computation. Our method can be extended by mapping the Rydberg qubit states used here to ground-state hyperfine sublevels, so that the entangled atoms can remain trapped and maintain their quantum coherence over very long times [22, 23, 27, 33]. This could enable the sophisticated manipulation of entanglement and realization of deep quantum circuits for applications such as quantum optimization [30, 31].

During the completion of this work, we became aware of related results demonstrating large GHZ state preparation using superconducting quantum circuits [34, 35].

ACKNOWLEDGMENTS

We thank Dries Sels and Christian Reimer for helpful discussions. The authors acknowledge financial support from the Center for Ultracold Atoms, the National Science Foundation, Vannevar Bush Faculty Fellowship, the US Department of Energy and the Office of Naval Research. H.L. acknowledges support from the National Defense Science and Engineering Graduate (NDSEG) fellowship. G.S. acknowledges support from a fellowship from the Max Planck/Harvard Research Center for Quantum Optics. J.C., S.M., and T.C. acknowledge funding from the EC H2020 grants 765267 (QuSCo), 817482 (PASQuANS), and QuantERA QTFLAG; the DFG SPP 1929 (GiRyd) and TWITTER; the IQST Alliance; and the Italian PRIN 2017.

* These authors contributed equally to this work
† To whom correspondence should be addressed; E-mail: lukin@physics.harvard.edu

[1] D. M. Greenberger, M. A. Horne, A. Zeilinger, *Bell's Theorem, Quantum Theory and Conceptions of the Universe*, M. Kafatos, ed., Fundamental Theories of Physics (Springer Netherlands, Dordrecht, 1989), pp. 69–72.
[2] L. Pezzè, A. Smerzi, M. K. Oberthaler, R. Schmied, P. Treutlein, *Rev. Mod. Phys.* **90**, 035005 (2018).
[3] M. A. Nielsen, I. L. Chuang, *Quantum Computation and Quantum Information: 10th Anniversary Edition* (Cambridge University Press, New York, NY, USA, 2011), 10th edn.

[4] L. Amico, R. Fazio, A. Osterloh, V. Vedral, *Rev. Mod. Phys.* **80**, 517 (2008).
[5] O. Gühne, G. Tóth, *Physics Reports* **474**, 1 (2009).
[6] R. Islam, *et al.*, *Nature* **528**, 77 (2015).
[7] C. A. Sackett, *et al.*, *Nature* **404**, 256 (2000).
[8] R. Laflamme, E. Knill, W. H. Zurek, P. Catasti, S. V. S. Mariappan, *Philosophical Transactions of the Royal Society of London. Series A: Mathematical, Physical and Engineering Sciences* **356**, 1941 (1998).
[9] P. Neumann, *et al.*, *Science* **320**, 1326 (2008).
[10] D. Bouwmeester, J.-W. Pan, M. Daniell, H. Weinfurter, A. Zeilinger, *Phys. Rev. Lett.* **82**, 1345 (1999).
[11] J.-W. Pan, M. Daniell, S. Gasparoni, G. Weihs, A. Zeilinger, *Phys. Rev. Lett.* **86**, 4435 (2001).
[12] X.-L. Wang, *et al.*, *Phys. Rev. Lett.* **120**, 260502 (2018).
[13] D. Leibfried, *et al.*, *Nature* **438**, 639 (2005).
[14] T. Monz, *et al.*, *Phys. Rev. Lett.* **106**, 130506 (2011).
[15] N. Friis, *et al.*, *Phys. Rev. X.* **8**, 021012 (2018).
[16] L. DiCarlo, *et al.*, *Nature* **467**, 574 (2010).
[17] C. Song, *et al.*, *Phys. Rev. Lett.* **119**, 180511 (2017).
[18] B. Vlastakis, *et al.*, *Science* **342**, 607 (2013).
[19] H. Labuhn, *et al.*, *Nature* **534**, 667 (2016).
[20] H. Bernien, *et al.*, *Nature* **551**, 579 (2017).
[21] D. Jaksch, *et al.*, *Phys. Rev. Lett.* **85**, 2208 (2000).
[22] T. Wilk, *et al.*, *Phys. Rev. Lett.* **104**, 010502 (2010).
[23] L. Isenhower, *et al.*, *Phys. Rev. Lett.* **104**, 010503 (2010).
[24] R. Islam, *et al.*, *Science* **340**, 583 (2013).
[25] N. Rach, M. M. Müller, T. Calarco, S. Montangero, *Phys. Rev. A* **92**, 062343 (2015).
[26] R. Heck, *et al.*, *PNAS* **115**, E11231 (2018).
[27] See Supplementary Materials
[28] S. de Léséleuc, D. Barredo, V. Lienhard, A. Browaeys, T. Lahaye, *Phys. Rev. A* **97**, 053803 (2018).
[29] M. Gärttner, *et al.*, *Nature Physics* **13**, 781 (2017).
[30] E. Farhi, J. Goldstone, S. Gutmann, *arXiv:1411.4028* (2014).
[31] L. Zhou, S.-T. Wang, S. Choi, H. Pichler, M. D. Lukin, *arXiv:1812.01041 [cond-mat, physics:quant-ph]* (2018).
[32] C. J. Turner, A. A. Michailidis, D. A. Abanin, M. Serbyn, Z. Papić, *Nature Physics* **14**, 745 (2018).
[33] C. J. Picken, R. Legaie, K. McDonnell, J. D. Pritchard, *Quantum Sci. Technol.* **4**, 015011 (2018).
[34] C. Song, *et al.*, *arXiv:1905.00320* (2019).
[35] K. X. Wei, *et al.*, *arXiv:1905.05720* (2019).

SUPPLEMENTARY MATERIALS

Experimental setup

The Rydberg excitations are enabled by a two-color laser system at 420 nm and 1013 nm wavelength. The 420 nm light is derived from a frequency-doubled titanium sapphire laser (M Squared SolsTiS 4000 PSX F) locked to an ultrastable reference cavity (by Stable Laser Systems). The 1013 nm light is obtained from a high-power fiber amplifier (ALS-IR-1015-10-A-SP by Azur Light Systems). The seed light is derived from a Fabry-Pérot laser diode injection locked to an external cavity diode laser (CEL002 by MOGLabs) stabilized to the same reference cavity and filtered by the cavity transmission [36]. The detuning of both Rydberg lasers to the intermediate state $|6P_{3/2}, F = 3, m_F = -3\rangle$ is approximately $2\pi \times 2\,\mathrm{GHz}$. The individual Rabi frequencies of the two Rydberg lasers are $\Omega_{420}/(2\pi) \approx 174\,\mathrm{MHz}$ and $\Omega_{1013}/(2\pi) \approx 115\,\mathrm{MHz}$. This gives a two-photon Rabi frequency of $\Omega = \Omega_{420}\Omega_{1013}/(2\Delta) \approx 2\pi \times 5\,\mathrm{MHz}$. We define the local phases of each atom's states $|0\rangle$ and $|1\rangle$ in the reference frame associated with the local phases of Rydberg excitation lasers, such that the two GHZ components have a relative phase $\phi = 0$ after state preparation.

To drive the optimal control pulses, we modulate the 420 nm Rydberg laser with an acousto-optic modulator (AOM) driven by an arbitrary waveform generator (AWG, M4i.6631-x8 by Spectrum). We correct the nonlinear response of the AOM to the drive amplitude by a feed-forward approach to obtain the target output intensity pattern. Furthermore, the AOM efficiency changes with changing frequency, which we compensate by feeding forward onto the waveform amplitude to suppress the intensity variations with frequency. In addition, the light shift on the Rydberg transition from the 420 nm laser can be as large as $2\pi \times 4\,\mathrm{MHz}$. While the pulse intensity changes, this light shift changes, modifying the detuning profile. We therefore correct the frequency profile as a function of the pulse intensity to compensate this shift. These steps ensure that the experimentally applied pulse is a faithful representation of the desired profile.

The local addressing beam patterns are generated by two AODs (DTSX400-800 by AA Opto-electronic), each driven by multiple frequencies obtained from an arbitrary waveform generator (M4i.6631-x8 by Spectrum).

Optimal control

Optimal control was originally developed as a tool to harness chemical reactions to obtain the largest amount of desired products with given resources, and then introduced in quantum information processing as a standard way of designing quantum protocols and quantum devices [37–40] as well as in manipulating quantum many-body systems to exploit complex phenomena [26, 41–49]. Quantum optimal control theory identifies the optimal shape of a time-dependent control pulse to drive a quantum many-body system to accomplish given task, e.g. state preparation or quantum gate implementation. The quality of the transformation is certified by a Figure of Merit (FoM) that can be calculated or measured, e.g. the fidelity of the final state with respect to the target one, the final occupation, or the energy.

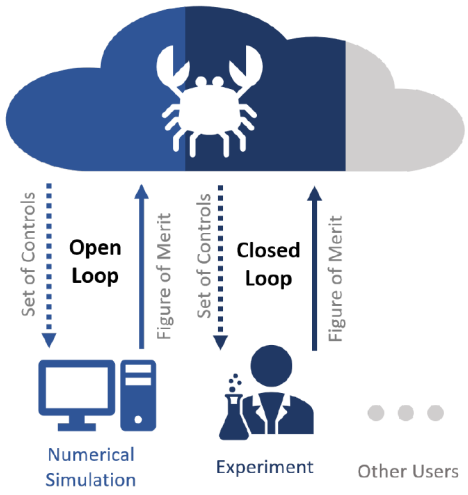

FIG. S1. RedCRAB optimization loop. The remote dCRAB server generates and transmits a trial set of controls to the user, who evaluates the corresponding performance in terms of a FoM and sends the feedback information to the server, concluding one iteration loop. In the next loop, the server tends to generate an improved set of controls based on previous feedback information. The optimization continues until it converges. The FoM evaluation can be achieved either by numerical calculation (open-loop optimization) or experimental measurement (closed-loop optimization).

In this work, the optimization is achieved through RedCRAB, the remote version of the dressed Chopped RAndom Basis (dCRAB) optimal control via a cloud server [26, 41, 48]. Within the optimization, control fields such as the Rabi coupling $\Omega(t)$ are adjusted as $\Omega(t) = \Omega_0(t) + f(t)$, where $\Omega_0(t)$ is an initial guess function obtained from physical intuition or existing suboptimal solutions. The correcting function $f(t)$ is expanded by randomized basis functions. In this work, we chose a truncated Fourier basis. Thus, $f(t) = \Gamma(t)\sum_{k=1}^{n_c}[A_k \sin(\omega_k t) + B_k \cos(\omega_k t)]$, where $\omega_k = 2\pi(k + r_k)/\tau$ are randomized Fourier frequencies with $r_k \in [-0.5, 0.5]$, τ is the final time, and $\Gamma(t)$ is a fixed scaling function to keep the values at initial and final times unchanged, i.e., $\Gamma(0) = \Gamma(\tau) = 0$. The optimization task is then translated into a search for the optimal combination of $\{A_k, B_k\}$ with a given r_k to maximize the fidelity

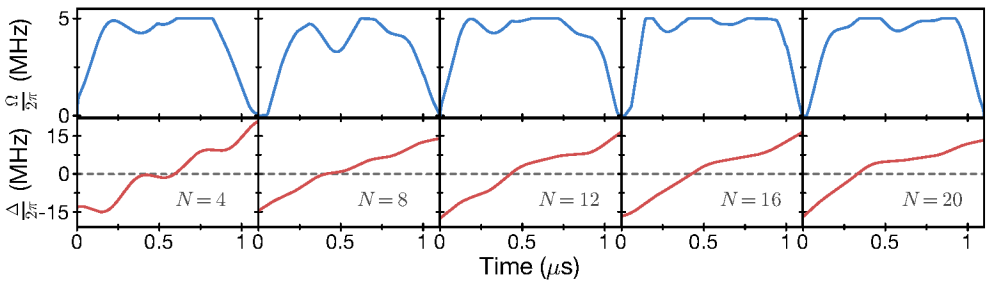

FIG. S2. Optimal control pulse diagrams. Shown are the Rabi frequency (top) and detuning profiles (bottom) for the different system sizes investigated here.

between the target state and the time evolved state at τ. It can be solved by iteratively updating $\{A_k, B_k\}$ using a standard Nelder-Mead algorithm [50]. In the basic version of the CRAB algorithm, all r_k are fixed and the local control landscape is explored for all n_c frequencies simultaneously. This leads to a restriction in the number of frequencies that can be efficiently optimised. Using the dressed CRAB (dCRAB) algorithm, only one Fourier frequency ω_k is optimised at a time. We then move on to ω_{k+1} after a certain number of iterations of the CRAB routine. This enables the method to include an arbitrarily large number of Fourier components and deriving the solutions without – whenever no other constraints are present – being trapped by local optima [25].

In the RedCRAB optimization, the server generates and transmits a trial set of controls to the client user, who will then evaluate the corresponding FoM and communicates the feedback information to the server finishing one iteration loop (Fig. S1). The optimization continues iteratively and the optimal set of controls, as well as the corresponding FoM are derived. In the RedCRAB optimization, the user can either evaluate the FoM by numerical calculation, namely open-loop optimization, or by experimental measurement, which is called closed-loop optimization. In this work, open-loop optimization was carried out only. The resulting controls could later serve as the initial guess for a future closed-loop optimization. This last step would ensure that the resulting controls are robust, since all unknown or not modelled experimental defects and perturbations would automatically be corrected for.

For the open-loop optimization of the pulse, we constrained the preparation time to 1.1 μs and allowed the detuning $\Delta/(2\pi)$ to vary between -20 MHz and 20 MHz, while $\Omega/(2\pi)$ could vary between $0-5$ MHz. The resulting pulses are shown in Fig. S2. While shorter pulses can work sufficiently well for smaller system sizes, we use an equal pulse duration for all N for better comparability. We find that the optimized pulses for larger systems appear smoother than for smaller system sizes, where the pulses bear less resemblance to an adiabatic protocol. However, the adiabaticity does not improve for larger system sizes, owing to the shrinking energy gaps.

Optimal control dynamics

To gain insight into the timescales required to prepare a GHZ state in our setup, we can compare our optimal control protocol with a minimal quantum circuit consisting of a series of two-qubit gates that would achieve the same task. In this circuit, a Bell pair is created in the first layer $p = 1$ in the middle of the array using the Rydberg blockade, which for our maximal coupling strength of $\Omega/(2\pi) = 5$ MHz takes $100\,\mathrm{ns}/\sqrt{2}$. The entanglement can be spread to the two atoms adjacent to this Bell pair by simultaneously applying a pair of local π pulses of 100 ns to those sites, corresponding to controlled rotations. A sequence of such gate layers $p = 2, ..., 10$, including operations on qubit pairs and the free evolution of other qubits, leads to the same GHZ state we prepare. This gate sequence requires approximately 1 μs, which is within 10% of the total evolution time required in our optimal control sequence, which builds up the entanglement in parallel. Furthermore, the fidelity of each layer of such a circuit effectively acting on all $N = 20$ qubits needs to be higher than 0.94 to achieve the 20-qubit GHZ fidelity demonstrated in this work.

It is interesting to compare this required evolution time with a parameter ramp that tries to adiabatically connect the initial state to the GHZ state. To this end, we parametrize the detuning and Rabi frequency as $\Delta(s) = (1-s)\Delta_0 + s\Delta_1$ and $\Omega(s) = \Omega_{\max}[1-\cos^{12}(\pi s)]$ respectively. A naïve (unoptimized) linear ramp of the detuning corresponds to choosing $s = t/T$. Alternatively, one can adjust the local ramp speed to minimize diabatic transitions, for example by choosing $s(t)$ minimizing

$$D = \left(\frac{ds}{dt}\right)^2 \sum_{n>0} \frac{|\langle E_n(s)|\partial_s H(s)|E_0(s)\rangle|^2}{(E_n(s)-E_0(s))^2}$$

during a ramp of duration T. Here $|E_n(s)\rangle$ are the instan-

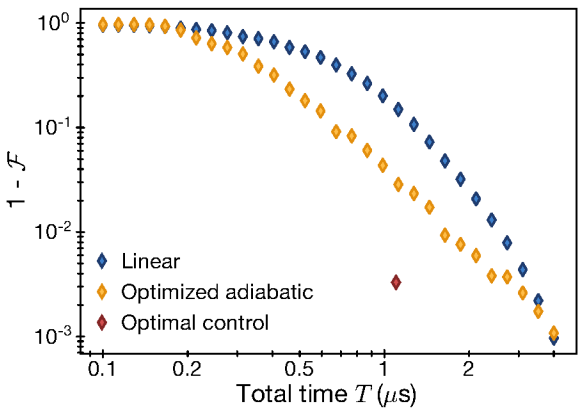

FIG. S3. Comparison of ramping profile fidelities. Comparison of linear ramps (blue) to optimized adiabatic ramps (orange) for $N = 12$ as a function of the total ramp time T. The optimal control pulse used in the experiment takes $T = 1.1$ μs and achieves a higher fidelity than either the linear ramp or the optimized adiabatic ramp.

taneous eigenstates of the Hamiltonian $H(s)$ specified by the parameters $\Omega(s)$ and $\Delta(s)$, with $|E_0(s)\rangle$ denoting the instantaneous ground state. In Fig. S3, we show the results of numerical simulations using both the linear sweep and a sweep that minimizes the strength of diabatic processes quantified by D. Both sweep profiles require larger total evolution time T than the optimal control pulse to reach similar fidelities.

To understand the origin of the speedup through optimal control, we numerically simulate the corresponding evolution and analyze the population of the instantaneous energy eigenstates (Fig. S4). The optimal control dynamics can be divided into three different regions: (I) A fast initial quench, (II) a slow quench, and (III) a fast final quench. Even though the change in the Hamiltonian parameters in region (I) is rather rapid, the system remains mostly in the instantaneous ground state, with negligible populations of the exited states, since the energy gap is large. In contrast, in region (II) the parameters change slows down, reflecting the fact that the energy gap becomes minimal. Unlike the adiabatic case however, one can observe nontrivial population dynamics, with a temporary population of excited states. Importantly, the optimal control finds a path in the parameter space such that the population is mostly recaptured in the ground state at the end of region (II). Finally, in region (III) the gap is large again and the system parameters are quickly changed to correct also for higher order contributions. This suggests that it actively uses diabatic transitions that go beyond the adiabatic principle. This mechanism is related to the recently discussed speedup in the context of the quantum approximate optimization algorithm (QAOA) [30, 31].

QUANTIFYING DETECTION

The many-body dynamics involving coherent excitation to Rydberg states occurs during a few-microsecond time window in which the optical tweezers are turned off. After the coherent dynamics, the tweezers are turned back on, and atoms in the ground state $|0\rangle$ are recaptured. However, there is a small but finite chance of losing these atoms. To quantify this error, we perform the GHZ state preparation experiment while disabling the 420 nm Rydberg pulse. This keeps all atoms in state $|0\rangle$, and we measure the loss probability to find a 0.9937(1) detection fidelity.

Atoms in state $|1\rangle$ on the other hand have a small chance of being misidentified as being in state $|0\rangle$, as these atoms can decay prematurely from the Rydberg state to the ground state and get recaptured by the tweezers. This error probability can be measured by preparing atoms at sufficiently large distances as to be non-interacting and applying a calibrated π pulse to transfer all atoms to $|1\rangle$ and measure the probability of recapturing them. However, part of this signal is given by the π pulse infidelity, i.e. a small fraction of atoms which did not get excited to $|1\rangle$ in the first place.

To quantify the π pulse fidelity, we note that a Rydberg atom that decays and is recaptured can decay either into the $F = 2$ or $F = 1$ ground states with branching ratios α and β, respectively ($\alpha + \beta = 1$). Our initial optical pumping of atoms into $|0\rangle$ has high fidelity > 0.998, measured using microwave spectroscopy on different sublevels of the $F = 2$ manifold. Thus, the final population of $F = 1$ atoms should be given only by Rydberg atom decay/recapture events. Following a π pulse to excite all atoms to the Rydberg state, the final measured population in $F = 1$ is $p_1 = p \times \beta$, where p is the total decay and recapture probability of a Rydberg atom. Meanwhile, the final measured population in $F = 2$ is $p_2 = p \times \alpha + \epsilon$, which includes both decay events from Rydberg atoms as well as residual population ϵ left from an imperfect π pulse. Experimentally, we separately measure the total recaptured ground state population $(p_1 + p_2)$, as well as the $F = 1$ population p_1 only (by a resonant push-out of $F = 2$ atoms). We additionally can vary the overall recapture probability p by changing the depth of the tweezers that we recapture atoms in, which changes the repulsive force exerted by the optical tweezers on Rydberg atoms [28]. We measure p_1 and $(p_1 + p_2)$ at four different total recapture probabilities to extract the π pulse infidelity as $\epsilon = 0.006(3)$ (Fig. S5). From these measurements, we conclude a Rydberg detection fidelity of 0.9773(42).

Detection errors of $|0\rangle$ can be mitigated by implementing ground-state cooling in the tweezers [51, 52], which reduces the probability of loss after releasing the atoms. The detection fidelity of $|1\rangle$ can be improved by using

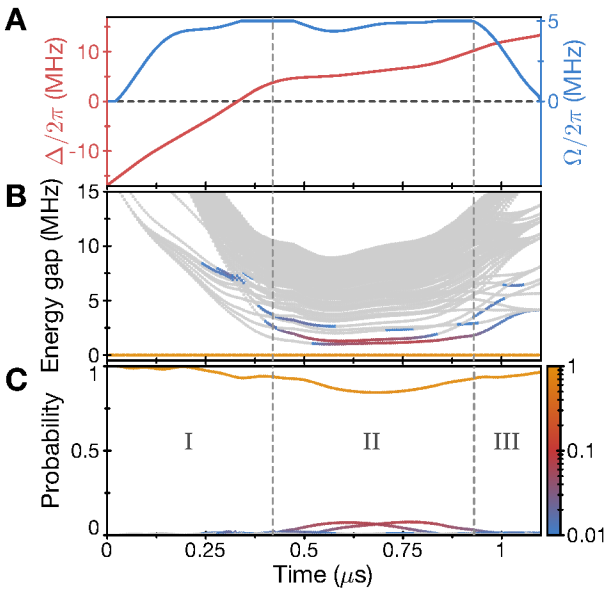

FIG. S4. Dynamics of an optimized 20-atom GHZ state preparation. **A,** Optimized control parameters $\Omega(t)$ and $\Delta(t)$ for $N = 20$ atoms. **B,** Energy eigenvalues of instantaneous eigenstates of the Hamiltonian relative to the ground state energy. The population in each energy eigenstate is color coded on a logarithmic scale. Light gray points correspond to populations smaller than 0.01. **C,** Probability in each instantaneous eigenstate as the initial state evolves under the time-dependent Hamiltonian. The probability is dominated by the ground state and a few excited states. The time evolution is computed by exact numerical integration of Schrödinger's equation, and 100 lowest energy eigenstates are obtained by using Krylov subspace method algorithms. For computational efficiency, we only consider the even parity sector of the Hamiltonian with no more than three nearest neighboring Rydberg excitations owing to the Rydberg blockade.

Rydberg states with a longer radiative lifetime, actively ionizing the Rydberg atoms by electric or optical fields, or by pulling them away from the trapping region with electric field gradients.

ACCOUNTING FOR DETECTION IMPERFECTIONS

The small imperfections in state detection of single qubits leads to a prominent effect on the analysis of large systems. The probability for a single detection error is sufficiently low that multiple errors per chain are very unlikely, and we observe that the reduction in probability of observing the correct GHZ pattern is dominated by these errors, as opposed to excitations of the system (Fig. S6A). This conclusion is further confirmed by noting that near-ideal correlations extend across the entire system (Fig. S7).

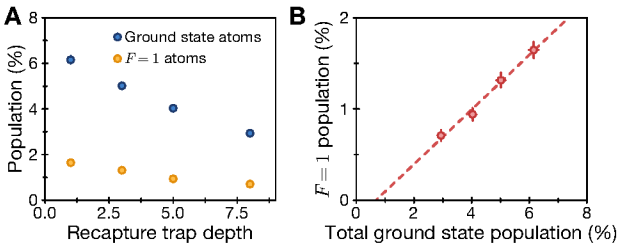

FIG. S5. Quantifying detection errors. **A,** Measurement of the recaptured Rydberg atoms in the ground state (blue points) and in the $F = 1$ ground-state manifold (orange points) as a function of the tweezer depth upon recapture. **B,** Recaptured populations in all ground state levels. The intersection with the horizontal axis gives an estimate of the atoms that were not excited to the Rydberg state, bounding the π pulse fidelity.

To properly infer the obtained fidelities, we account for these imperfections using the following procedure:

Coherences: The coherences are extracted from the amplitude of parity oscillations. Each point in the parity oscillation is analyzed from the measured distribution of the number of excitations in the system. We encode this measured probability distribution in the vector $\mathbf{W}$, where W_n is the probability to observe exactly n excitations in the system ($0 \leq n \leq N$). The true probability distribution of excitation numbers, prior to the effect of detection errors, is denoted $\mathbf{V}$. Detection errors transform this distribution according to a matrix M, where M_{mn} encodes the probability that a state with n excitations will be detected as having m excitations. Each matrix element is calculated using combinatoric arguments from the measured detection fidelities. We determine the true distribution $\mathbf{V}$ as the one that minimizes the cost function $|M\mathbf{V} - \mathbf{W}|^2$. (Fig. S6B). This procedure is similar to applying the inverse matrix M^{-1} to the measured distribution $\mathbf{W}$, but is more robust in the presence of statistical noise on the measured distribution. Error bars on the inferred values are evaluated by random sampling of detection fidelities, given our measured values and uncertainties.

Populations: We carry out a similar procedure for the population data; however, we are interested in assessing the probability of two particular target states, which are defined not only by their number of excitations but also by their staggered magnetizations $M_n = \sum_{i=1}^{N}(-1)^i\langle\sigma_z^{(i)}\rangle$. Our procedure therefore operates by grouping all possible microstates according to their common staggered magnetization and number of excitations (Fig. S6C). For N particles, there are in general $(N/2+1)^2$ such groups. As before, we denote the raw measured distribution with respect to these groups as $\mathbf{W}$. We construct a detection error matrix M that redistributes populations between groups according to the

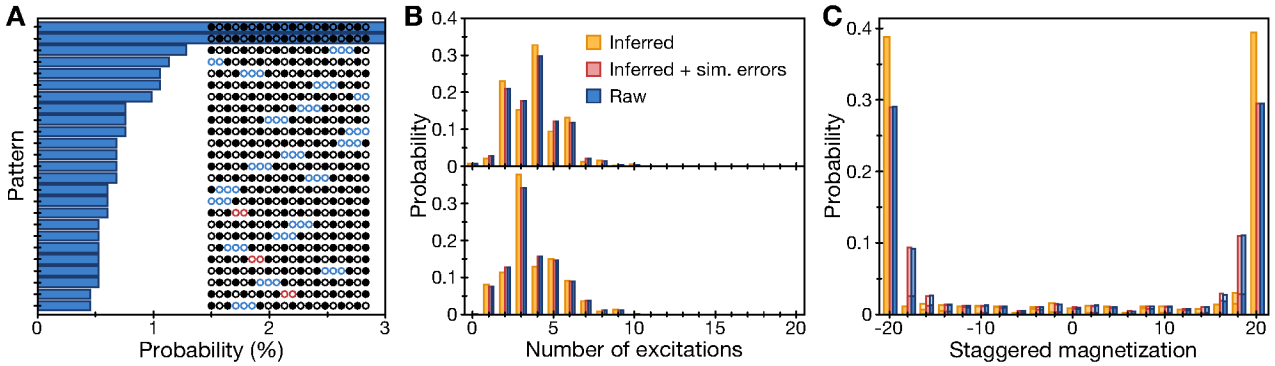

FIG. S6. Inference of parity and populations. **A,** Histogram of observed patterns after preparing a 20-atom GHZ state. Open circles denote atoms in $|0\rangle$ and filled circles denote atoms in state $|1\rangle$. Blue domains mark regions where a single detection error has likely occurred, since such patterns are energetically costly at large positive detuning of the Rydberg laser. Red domains mark true domain walls, where the antiferromagnetic order is broken. Following the correct GHZ patterns, the 14 most observed patterns are consistent with a single detection error. **B,** Distribution of number of excitations measured for two different times of the parity oscillation for a 20-atom array, with the upper (lower) plot at $\phi = 0$ ($\phi = \pi/20$) of phase accumulation per atom, showing a net positive (negative) parity. Blue bars show directly measured values, orange bars show the statistically inferred parent distribution, and red bars denote the parent distribution after adding simulated errors to compare to the raw data. **C,** Staggered magnetization M_n extracted from the measurement of GHZ populations for 20 atoms. The vertically split bars with different shading denote different occurrences of number of excitations.

measured detection error rates. We optimize over all possible true distributions to find the inferred distribution $\mathbf{V}$ that minimizes the cost function $|M\mathbf{V} - \mathbf{W}|^2$. Following this procedure, we sum the populations in the two groups that uniquely define the two target GHZ components with a staggered magnetization of $\pm N$, and $N/2$ excitations.

Bounding the GHZ state coherence

We expand an experimental GHZ-like density matrix in the following form

$$\begin{aligned}\rho =&\alpha_1 |A_N\rangle\langle A_N| + \alpha_2 |\overline{A}_N\rangle\langle\overline{A}_N| \\ &+ \left(\beta |A_N\rangle\langle\overline{A}_N| + \beta^* |\overline{A}_N\rangle\langle A_N|\right) + \rho'\end{aligned} \tag{1}$$

where $|A_N\rangle = |0101\cdots\rangle$ and $|\overline{A}_N\rangle = |1010\cdots\rangle$ are the target GHZ components, α_i characterizes the diagonal populations in these states ($0 \leq \alpha_i \leq 1$), β characterizes the off-diagonal coherence between these states ($0 \leq |\beta| \leq 1/2$), and ρ' contains all other parts of the density matrix. The GHZ fidelity of state ρ is given by:

$$\mathcal{F} = \langle \mathrm{GHZ}_N | \rho | \mathrm{GHZ}_N \rangle = \frac{\alpha_1 + \alpha_2}{2} + \mathrm{Re}(\beta) \tag{2}$$

To measure the coherence $|\beta|$, we implement a staggered magnetic field to which the target GHZ state is maximally sensitive:

$$H_{\mathrm{st}} = \frac{\hbar\delta}{2} \sum_{i=1}^{N} (-1)^i \sigma_z^{(i)} \tag{3}$$

Applying H_{st} to the system for time T results in unitary phase accumulation $U(T) = \exp(-iH_{\mathrm{st}}T/\hbar)$. We then apply a unitary $\mathcal{U}$ to the system and measure in the computational basis. From repeated measurements, we calculate the expectation value of the global parity operator $\mathcal{P} = \prod_i \sigma_z^{(i)}$ as a function of the phase accumulation time T. Denote the time-dependent expectation value $E(T)$, where $-1 \leq E(T) \leq 1$.

We show that if $E(T)$ has a frequency component that oscillates at a frequency of $N\delta$, then the amplitude of this frequency component sets a lower bound for $|\beta|$. Importantly, this holds for any unitary $\mathcal{U}$ used to detect the phase accumulation.

Proof: The expectation value $E(T)$ can be written explicitly as the expectation value of the time-evolved observable $\mathcal{P} \to U^\dagger(T)\mathcal{U}^\dagger\mathcal{P}\mathcal{U}U(T)$. In particular,

$$\begin{aligned}E(T) &= \mathrm{Tr}[\rho U^\dagger(T)\mathcal{U}^\dagger\mathcal{P}\mathcal{U}U(T)] \\ &= \sum_n \langle n| \rho U^\dagger(T)\mathcal{U}^\dagger\mathcal{P}\mathcal{U}U(T) |n\rangle\end{aligned} \tag{4}$$

where $|n\rangle$ labels all computational basis states. Since the phase accumulation Hamiltonian H_{st} is diagonal in the computational basis, the basis states $|n\rangle$ are eigenvectors of $U(T)$ with eigenvalues denoting the phase accumulation. Specifically,

$$H_{\mathrm{st}} |n\rangle = \frac{\hbar\delta}{2} M_n |n\rangle \Rightarrow U(T) |n\rangle = e^{-i\delta T M_n/2} |n\rangle \tag{5}$$

where M_n is the staggered magnetization of state $|n\rangle$ defined earlier. The staggered magnetization of the state

$|A_N\rangle$ is maximal: $M_{A_N} = N$, and the staggered magnetization of $|\overline{A}_N\rangle$ is minimal: $M_{\overline{A}_N} = -N$. Note that all other computational basis states have strictly smaller staggered magnetizations. Inserting an identity operator in Eq. (4):

$$\begin{aligned} E(T) =& \sum_{n,m} \langle n|\,\rho\,|m\rangle\langle m|\,U(T)^\dagger \mathcal{U}^\dagger \mathcal{P}\mathcal{U} U(T)\,|n\rangle \\ =& \sum_{n,m} e^{-i\delta T(M_n - M_m)/2}\,\langle n|\,\rho\,|m\rangle\langle m|\,\mathcal{U}^\dagger\mathcal{P}\mathcal{U}\,|n\rangle \end{aligned} \tag{6}$$

The highest frequency component comes from the states with maximally separated staggered magnetization, $|n\rangle = |A_n\rangle$ and $|m\rangle = |\overline{A}_n\rangle$. Separating out this frequency component as $F(T)$, we obtain:

$$\begin{aligned} F(T) =& 2\mathrm{Re}\left[e^{-iN\delta T}\,\langle A_N|\,\rho\,|\overline{A}_N\rangle\langle\overline{A}_N|\,\mathcal{U}^\dagger\mathcal{P}\mathcal{U}\,|A_N\rangle\right] \\ =& 2\mathrm{Re}\left[\beta e^{-iN\delta T}\,\langle\overline{A}_N|\,\mathcal{U}^\dagger\mathcal{P}\mathcal{U}\,|A_N\rangle\right] \end{aligned} \tag{7}$$

We note that the parity matrix element is bounded as $0 \le \left|\langle\overline{A}_N|\mathcal{U}^\dagger\mathcal{P}\mathcal{U}|A_N\rangle\right| \le 1$. Furthermore, the matrix element is real-valued and positive for the unitary $\mathcal{U}$ considered in the experiment. Fitting $F(T)$ to an oscillation with amplitude $C \ge 0$ and phase ϕ according to $F(T) = C\cos(N\delta T - \phi)$, we produce our lower bound for the off-diagonal coherence β:

$$|\beta| \ge C/2; \quad \arg(\beta) = \phi \tag{8}$$

Parity detection

The ideal observable to measure GHZ phase is the parity $\mathcal{P}_x = \prod_i \sigma_x^{(i)}$. However, the presence of Rydberg interactions and the Rydberg blockade prevents us from rotating all qubits such that we can measure in this basis. Instead, in this work we generate a unitary $\mathcal{U}_x = \exp\left(-i\Omega t/2\sum_i \sigma_x^{(i)} - iH_{\mathrm{int}}t/\hbar\right)$ by resonantly driving all atoms in the presence of these interactions given by H_{int} for a fixed, optimized time (Fig. S8), and subsequently measure the parity $\mathcal{P} = \prod_i \sigma_z^{(i)}$ in the computational basis. The finite duration of the unitary $\mathcal{U}_x$ incurs a small amount of additional infidelity, owing both to dephasing and an additional laser scattering. However, we estimate that this effect should only lead to small losses in fidelity on the percent level.

While it is not obvious that the parity observable used here is suitable, we can understand the parity oscillations in the picture of weakly interacting spin-1 particles defined on dimers of neighboring pairs of sites. For two adjacent sites, we can define eigenstates of a spin-1 S_z operator as $|\circ\bullet\rangle = |-\rangle$, $|\circ\circ\rangle = |0\rangle$, and $|\bullet\circ\rangle = |+\rangle$. In this notation, the antiferromagnetic GHZ state we prepare is given by a ferromagnetic GHZ state in the spin-1 basis:

$$|\mathrm{GHZ}_N\rangle = \frac{1}{\sqrt{2}}\left(|++\cdots\rangle + |--\cdots\rangle\right) \tag{9}$$

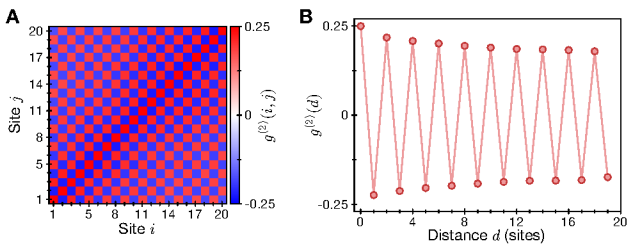

FIG. S7. Density-density correlations for a 20-atom GHZ state. **A**, We evaluate the correlation function $g^{(2)}(i,j) = \langle n_i n_j\rangle - \langle n_i\rangle\langle n_j\rangle$ and observe strong correlations of Rydberg excitations across the entire system. **B**, The density-density correlations over distance, given by $g^{(2)}(d) \propto \sum_i g^{(2)}(i,i+d)$ decay only very slowly throughout the array.

We must express all operations on the GHZ state in this new notation. In particular, the transverse field of the form $\hbar\Omega/2\sum_i \sigma_x^{(i)}$ applied to individual atoms gets transformed to an operation $\hbar\Omega/\sqrt{2}\sum_j S_x^{(j)}$ on all dimers. Furthermore, the staggered field $\hbar\delta/2\sum_i(-1)^i\sigma_z^{(i)}$ we apply to individual atoms to rotate the GHZ phase is equivalent to an operation of the form $\hbar\delta\sum_j S_z^{(j)}$ acting on individual dimers.

The parity operator in the single-qubit basis $\mathcal{P} = \prod_i \sigma_z^{(i)}$ can be transformed into the dimer basis as

$$\mathcal{P} = \prod_j \left(-|+\rangle\langle+|_j - |-\rangle\langle-|_j + |0\rangle\langle 0|_j\right) \tag{10}$$

by noting that the three dimer states are eigenstates of $\mathcal{P}$, i.e. $\mathcal{P}\,|\pm\rangle = -|\pm\rangle$ and $\mathcal{P}\,|0\rangle = |0\rangle$.

Assuming we begin from a GHZ state, applying a rotation on all dimers for a duration given by $\Omega t = \pi/\sqrt{2}$ saturates the difference in $\mathcal{P}$ between GHZ states of opposite phase. This shows that such a protocol would be optimal if the dimer approximation were exact. However, interactions between dimers cannot be neglected. In particular, the Rydberg blockade suppresses configurations of the form $|\cdots--+\cdots\rangle$ owing to the strong nearest-neighbor interaction V, and neighboring dimers of the same type such as $|\cdots\pm\pm\cdots\rangle$ have a weak interaction given by the next-to-nearest neighbor interaction strength $V_2 = V/2^6$. We can thus express the interactions in the system as

$$\begin{aligned} \frac{H_{\mathrm{int}}}{\hbar} =& \sum_{j=1}^{N/2-1} V_2\,|+\rangle\langle+|_j\,|+\rangle\langle+|_{j+1} + V_2\,|-\rangle\langle-|_j\,|-\rangle\langle-|_{j+1} \\ &+ V\,|-\rangle\langle-|_j\,|+\rangle\langle+|_{j+1} \end{aligned} \tag{11}$$

An exact simulation of the dimer rotation under the interaction Hamiltonian (11) shows that both these interaction effects reduce the parity contrast by a small amount. In the recently discussed context of quantum many-body scars [20, 32, 53, 54], these effects of residual interactions

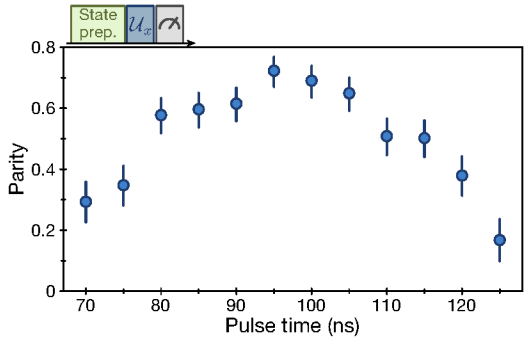

FIG. S8. Parity signal measured as a function of the time the operation $\mathcal{U}_x$ is applied. The total time includes delays in the AOM response and the finite laser pulse rise time.

lead of small deviations from a stable periodic trajectory through phase space.

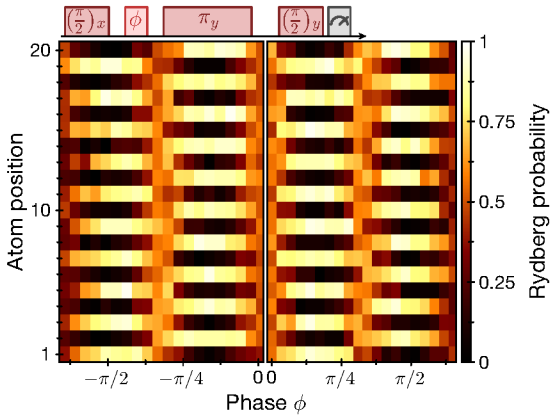

FIG. S9. Phase accumulation measured on an array of 20 sites. The left panel demonstrates application of a negative staggered field by applying local addressing beams on the odd sites in the array. The right panel shows a positive staggered field by instead applying local addressing beams on the even sites in the array. Phase is accumulated on each site at a rate of $2\pi \times 3.8$ MHz.

Staggered field calibration

To apply the staggered field (3), we address each of the even sites in the array with a focused off-resonant laser beam at 420 nm. However, the unitary in question requires a staggered field with opposite sign on every site. We compensate for the missing acquired phase on the sites in between the addressed ones by shifting the phase of the Rydberg laser, through a change in phase of the radio-frequency drive of the AOM. The intensity of each addressing beam is measured by applying a spin-echo sequence with an addressing pulse of variable duration to determine the light shift on the Rydberg transition. We correct for inhomogeneous intensities so that all atoms are subject to the same light shift.

We measure and calibrate the staggered field by measuring the effect of the field on each atom individually. To do so, we alternately rearrange the atoms to form different subsets of the 20-atom system that are sufficiently far apart to avoid interactions between them. In this configuration, every atom is then subject to a $\pi/2$ rotation about the x-axis, followed by the staggered field for variable duration, then a $\pi/2$ rotation about the y-axis, to distinguish positive from negative phase evolution. With an additional π rotation about the y-axis, we perform a spin echo to mitigate effects of dephasing. The outcome of this protocol is shown in Fig. S9 and demonstrates the implementation of the staggered magnetic field. By switching the local addressing beams to the opposite set of alternating sites, we switch the sign of the staggered field, enabling the measurement of both positive and negative phase accumulation.

Measured GHZ fidelities

For each system size N, we measure the GHZ populations and the GHZ coherence by parity oscillations (Figs. 2, 3 of the main text). From the raw measurements, we infer the true GHZ fidelity using the maximum likelihood procedure discussed in Section "Accounting for detection imperfections". All measured values are shown in table S1. Error bars on raw populations represent a 68% confidence interval for the measured value. Error bars on the raw coherences are fit uncertainties from the parity oscillations. Error bars on the inferred values include propagation of the uncertainty in the estimation of the detection fidelities.

Experimental Imperfections

We identify a number of experimental imperfections that to varying degrees can limit the coherent control of our atomic system.

1. **Atomic temperature:** The atom temperature of $\sim 10\,\mu$K leads to fluctuating Doppler shifts in the addressing lasers of order $\sim 2\pi \times 43$ kHz, as well as fluctuations in atomic position that leads to variation in Rydberg interactions strengths. These fluctuations are included in the simulations shown in the main text Fig. 3. These effects can be dramatically reduced by improved atomic cooling, most notably by sideband cooling within the optical tweezers to the motional ground state [51, 52].

System size N	4	8	12	16	20
Raw populations	0.893(6)	0.797(8)	0.695(9)	0.629(12)	0.585(14)
Inferred	0.946(10)	0.892(17)	0.824(21)	0.791(29)	0.782(32)
Raw coherence	0.710(12)	0.516(11)	0.371(10)	0.282(11)	0.211(11)
Inferred	0.759(11)	0.598(16)	0.462(19)	0.373(19)	0.301(18)
Raw fidelity	0.801(7)	0.657(7)	0.533(7)	0.455(8)	0.398(9)
Inferred	0.852(7)	0.745(12)	0.643(14)	0.582(17)	0.542(18)

TABLE S1. Measured GHZ data for all system sizes. Errors denote 68% confidence intervals.

2. **Laser scattering:** The two-photon excitation scheme to our chosen Rydberg state leads to off-resonant scattering from the intermediate state, $6P_{3/2}$. This scattering rate has a timescale of $50-100\mu$s for the two laser fields, and can be reduced by higher laser powers and further detuning from the intermediate state.

3. **Rydberg state lifetime:** The $70S$ Rydberg state has an estimated lifetime of 150 μs [55], limited both by radiative decay and blackbody-stimulated transitions. This effect could be mitigated by selecting a higher Rydberg state with a longer lifetime or by cryogenic cooling of the blackbody environment.

Additional error sources that may limit our coherence properties include laser phase noise, which can be mitigated by better laser sources and stabilization schemes, and fluctuations in local addressing beam intensities and positions, which can be addressed by active feedback on the beam positions and improved thermal and mechanical stability of the setup. Simulations predict that we could go beyond the system sizes studied here. While GHZ states of $N = 24$ could be within reach with current parameters, generation of even larger GHZ states should be feasible with the additional technical improvements discussed above.

GROUND-STATE QUBIT ENCODING

The GHZ state parity could be more easily detected and manipulated if the qubits were encoded in a basis of hyperfine sublevels of the electronic ground state. In particular, one can consider two alternative qubit states $|\tilde{0}\rangle = |5S_{1/2}, F = 1, m_F = -1\rangle$ and $|\tilde{1}\rangle = |5S_{1/2}, F = 2, m_F = -2\rangle$. Rotations between these states are possible through stimulated Raman transitions or microwave driving, and the interactions are introduced by coupling $|\tilde{1}\rangle$ to a Rydberg level $|r\rangle$. This type of hyperfine encoding has been employed in multiple experiments with cold Rydberg atoms [22, 23, 33]. To prepare GHZ states in this basis, all atoms can be initialized in $|\tilde{1}\rangle$ and the system transferred to the state $|\tilde{1}r\tilde{1}r\cdots\rangle + |r\tilde{1}r\tilde{1}\cdots\rangle$ using the method described in this work. A ground-state qubit π pulse followed by a π pulse on the Rydberg transition transforms the state into $|\tilde{0}\tilde{1}\tilde{0}\tilde{1}\cdots\rangle + |\tilde{1}\tilde{0}\tilde{1}\tilde{0}\cdots\rangle$, enabling the long-lived storage of entanglement. Additionally, local qubit rotations can flip the state of every other site to prepare the canonical form of the GHZ state, $|\tilde{0}\tilde{0}\tilde{0}\cdots\rangle + |\tilde{1}\tilde{1}\tilde{1}\cdots\rangle$, which can achieve entanglement-enhanced metrological sensitivity to homogeneous external fields [2]. Incorporating this type of hyperfine qubit encoding with Rydberg qubit control will be important for realizing quantum gates and deeper quantum circuits in future experiments.

* These authors contributed equally to this work
† To whom correspondence should be addressed; E-mail: lukin@physics.harvard.edu

[36] H. Levine, *et al.*, *Phys. Rev. Lett.* **121**, 123603 (2018).
[37] S. Montangero, T. Calarco, R. Fazio, *Phys. Rev. Lett.* **99**, 170501 (2007).
[38] C. Brif, R. Chakrabarti, H. Rabitz, *New J. Phys.* **12**, 075008 (2010).
[39] J. Cui, F. Mintert, *New J. Phys.* **17**, 093014 (2015).
[40] C. P. Koch, *J. Phys.: Condens. Matter* **28**, 213001 (2016).
[41] P. Doria, T. Calarco, S. Montangero, *Phys. Rev. Lett.* **106**, 190501 (2011).
[42] S. J. Glaser, *et al.*, *Eur. Phys. J. D* **69**, 279 (2015).
[43] I. Brouzos, *et al.*, *Phys. Rev. A* **92**, 062110 (2015).
[44] S. Lloyd, S. Montangero, *Phys. Rev. Lett.* **113**, 010502 (2014).
[45] S. van Frank, *et al.*, *Scientific Reports* **6**, 34187 (2016).
[46] M. M. Müller, *et al.*, *Phys. Rev. A* **87**, 053412 (2013).
[47] T. Caneva, *et al.*, *Phys. Rev. Lett.* **103**, 240501 (2009).
[48] T. Caneva, T. Calarco, R. Fazio, G. E. Santoro, S. Montangero, *Phys. Rev. A* **84**, 012312 (2011).
[49] J. Cui, R. van Bijnen, T. Pohl, S. Montangero, T. Calarco, *Quantum Sci. Technol.* **2**, 035006 (2017).
[50] J. A. Nelder, R. Mead, *Comput J* **7**, 308 (1965).
[51] A. M. Kaufman, B. J. Lester, C. A. Regal, *Phys. Rev. X* **2**, 041014 (2012).
[52] J. D. Thompson, T. G. Tiecke, A. S. Zibrov, V. Vuletic, M. D. Lukin, *Phys. Rev. Lett.* **110**, 133001 (2013).
[53] V. Khemani, C. R. Laumann, A. Chandran, *Phys. Rev. B* **99**, 161101 (2019).

[54] W. W. Ho, S. Choi, H. Pichler, M. D. Lukin, *Phys. Rev. Lett.* **122**, 040603 (2019).
[55] I. I. Beterov, I. I. Ryabtsev, D. B. Tretyakov, V. M. Entin, *Phys. Rev. A* **79**, 052504 (2009).